1987

NASA/ASEE SUMMER FACULTY FELLOWSHIP PROGRAM

MARSHALL SPACE FLIGHT CENTER
THE UNIVERSITY OF ALABAMA

COMPUTER-AIDED ANALYSIS FOR THE MECHANICS OF GRANULAR MATERIALS (MGM) EXPERIMENT, PART 2

Prepared by:	Joey K. Parker, Ph.D.
Academic Rank:	Assistant Professor
University and Department:	The University of Alabama Mechanical Engineering Department
NASA/MSFC:	
Laboratory:	Systems Dynamics
Division:	Atmospheric Sciences
Branch:	Fluid Dynamics
MSFC Colleague:	Nicholas C. Costes, Ph.D.
Date:	July 17, 1987
Contract No.:	The University of Alabama in Huntsville NGT-01-008-021

Abstract

Computer vision based analysis for the MGM experiment is continued and expanded into new areas. Volumetric strains of granular material triaxial test specimens have been measured from digitized images. A computer-assisted procedure is used to identify the edges of the specimen, and the edges are used in a three-dimensional model to estimate specimen volume. The results of this technique compare favorably to conventional measurements. A simplified model of the magnification caused by diffraction of light within the water of the test apparatus was also developed. This model yields good results when the distance between the camera and the test specimen is large compared to the specimen height. An algorithm for a more accurate three-dimensional magnification correction is also presented. The use of composite and RGB color cameras is discussed and potentially significant benefits from using an RGB camera are presented.

Acknowledgements

The author would like to thank his NASA colleague, Dr. Nicholas C. Costes for the opportunity to conduct this research, and for his help during the last two summers. Thanks are also due for his associate, Dr. C. J. Shin of the University of Colorado, for his many useful suggestions and assistance with the experimental apparatus.

Introduction

Civil engineers have conducted triaxial tests on soil specimens for many years. These tests are used to determine stress-strain relationships as well as specimen volume changes during axial compression or extension. The mechanical behavior of soils and other granular materials is important in the design of building foundations, bridges, dams, and other civil engineering applications. Another important characteristic of soils is their behavior during earthquakes.

One limitation of current triaxial testing methods is that the uniform confining pressure applied to a cylindrical soil specimen must be above a level of approximately 7-13 kPa (1-2 psi). Below this pressure threshold the weight of the specimen causes non-uniform stresses and deformations from the top to the bottom. However, during an earthquake the confining pressure can drop to essentially zero. One purpose of the Mechanics of Granular Materials Experiment (MGM) is to use the micro-gravity environment of the Space Shuttle to allow triaxial testing of granular materials under low confining pressures of less than 7 kPa (1 psi). Conventional measurements of axial loads and displacements, confining pressure, and pore pressure of the granular material specimen will be regularly recorded during a Shuttle flight. Video recordings of three views of the specimen uniformly spaced around the periphery will also be made. The video recordings have three major uses:

1) give visual confirmation of the presence (or absence) of "shear bands" in the specimen,
2) allow the precise tracking of several "tracer" particles scattered throughout the granular material, and
3) provide an alternate means for determining volume changes within the specimen.

This project is primarily concerned with the last two uses given above. Work conducted last summer [Parker, '86] concentrated on the tracking of individual tracer particles. That effort is continued in this report, and the measurement of volume changes is also considered.

Computer vision is used to perform these additional analyses for triaxial tests on granular materials. A "frame grabber" is used to digitize the recorded video signal for subsequent computer processing. A set of interactive computer programs has been written to assist the data analyst in evaluating the experiments.

Objectives

The primary objective of this project is to develop techniques for analyzing digitized images of granular material triaxial tests. Within this primary objective are several specific objectives:

1) continue development of tracer bead tracking,
2) develop a means for detecting and analyzing tracer beads that "touch" one another,
3) generate procedure to correct for magnification of the test specimen due to diffraction of light within the water/confining chamber system, and
4) measure volumetric strain from the digitized images.

A secondary objective is to develop methods for generating hardcopies of the digitized images.

Hardware & Equipment

The computer vision system uses an Imaging Technology PCVision Frame Grabber accessory board. The frame grabber is installed in an IBM PC AT microcomputer (with a 6 MHz Intel 80286 microprocessor). The PCVision board effectively digitizes a standard RS-170 television signal into a 512 column by 480 row pixel (picture element) matrix with a resolution of 8 bits (2^8 = 256 gray levels). A standard composite color camera (JVC #BY-110) and an electronic CCD (charge coupled device) camera (Micro-Technica #M-852) were both used for viewing the experimental setup. The CCD camera delivered both composite color output and separate RGB (red-green-blue) outputs.

Several different granular material specimens were used. Most were from 0.05 to 0.1 m (2 to 4 inches) in diameter and from 0.08 to 0.15 m (3 to 6 inches) tall. The granular materials used were either 3 mm diameter glass beads, "Ottawa" sand, or #20 silica sand. All specimens are constrained by a thin translucent latex membrane which tends to blur the details of the specimen. The specimen is placed inside a clear plastic pressure chamber cylinder of approximately 0.15 m (6 inch) inside diameter. The annular region between the specimen and the clear outer cylinder is filled with water, which is externally pressurized to maintain a constant confining pressure. Figure 1 shows a photograph of the test apparatus. The test specimen in Figure 2 consists of red and blue 3 mm diameter glass beads.

Volume Change Measurement

One of the important measurements desired from a triaxial test is the per cent volume change as a function of axial strain. Test specimens are carefully compacted to a uniform desired density prior to testing. Density is calculated from the measured volume and weight of the specimen. The standard method for determining volume changes during the test is to measure the amount of water displaced from the confining chamber. With a known initial volume the per cent volume change can then be determined.

There are two potential sources of error with this conventional method for determining volumetric strain. The volume of the specimen can change slightly (2-3%) between the time of density measurement and actual testing. Since the maximum per cent volume change during the test is approximately 7-10%, an alternative procedure is desired. Also, during an undrained triaxial test with a saturated specimen (voids between granular material are filled with water) the phenomenon of "membrane penetration" can occur. The pressure of the confined water in the test specimen increases when the specimen compacts during axial compression. This increased pressure causes the membrane to separate from the test specimen. The water displaced from the confining chamber depends on the volume inside the membrane, and no longer accurately represents the specimen volume change. If the video system can directly measure the specimen volume, this source of error may be eliminated.

Since volume is a three-dimensional property of the specimen, using two-dimensional video images for measurement causes some problems. First, since only a projection of the surface of the specimen is viewed, a model must be selected for mapping this projection into a three-dimensional volume. The results of the image-based volume measurement depend greatly on how well the conditions of the model are satisfied by the actual specimen throughout the test. Secondly, the magnification effects caused by the diffraction of light in the water between the specimen and the confining chamber must be accounted for. Both of these considerations are discussed along with several comparisons to data obtained from the conventional measurement technique.

Three-dimensional Model

The model chosen for mapping the two-dimensional image to a three dimensional solid is a series of circular disks stacked one atop the other. Only the diameter and height of each disk must be known in order to determine volume. The

height of each disk was assumed to be one vertical pixel in the observed image. The model does not require that the disks form a concentric stack. Therefore, the diameter for each disk can be determined if the left and right edges of the specimen are found at each vertical pixel location.

One way to determine the edges of the specimen is to manually trace them with a pointer on the screen. A simple program to accomplish this was written and evaluated. A "mouse" was used to move a cursor which overlayed the specimen image on the video screen. The cursor left a "trail" of black pixels marking the edge. This process was very tedious and prone to errors after a few images were analyzed. The main benefit is that the operator can be quite confident that the exact edge of the specimen is marked, if sufficient care and patience are used.

Computer detection of edges in digitized images has been studied for several years by many researchers. An overview of edge detection techniques is given in [Pratt, '78] and [Abdou and Pratt, '79]. Most of these techniques produce a new image in which edge pixels are enhanced and non-edge pixels are suppressed. The Robert's operator [Roberts, '65] is a relatively simple 2x2 nonlinear cross operation for sharpening edges. The Sobel [Duda and Hart, '73], Prewitt [Prewitt, '70] and the Kirsch [Kirsch, '71] operators all use 3x3 nonlinear operations and give similar performance in detecting edges. All of these operators use small regions (3x3 pixels or less) and are essentially first derivative approximations. They are also quite sensitive to noise, i.e., an image with spot noise will produce many false edges.

The trend in edge detection for the last several years has been to use larger areas to reduce the effects of noise. The Marr-Hildreth zero crossing of Laplacian [Marr and Hildreth, '80] and the 11x11 directional derivative operator [Haralick, '84] are both second derivative operations. These operators have one benefit in that thresholding is replaced by zero crossing for edge detection. The fact that they use large areas (11x11 pixels) makes them computationally slow and difficult. The six operators of the linear feature extraction algorithm [Nevatia and Babu, '80] use 5x5 areas and appear to strike a good compromise between noise rejection and computational ease. The latest in edge detection is the blur-minimum morphologic edge operator [Lee, Haralick, and Shapiro, '87] which uses either 3x3, 5x5, or larger areas. Figure 3 shows an application of this operator to the typical specimen image. The primary benefit of this operator is good noise rejection even with small regions.

Observation of Figure 3 indicates a major problem for the detection of the edges of the granular material specimen: too many "edges" are found. All of the edge operators developed to date use a localized operator which manipulates pixel intensities to locate regions of high contrast. Unfortunately, the digitized images of the specimens have many areas where relatively high contrast can occur due to shadows, uneven lighting, tracer beads, etc. The problem becomes especially acute during the latter stages of the triaxial test when the latex membrane starts to buckle and fold creating many false edges.

To overcome these problems a program was developed (ASSIST.PAS) which combines features of both manual and computerized edge detection. The program presents the digitized image on the screen with cursors for manually identifying the top and bottom edges of the specimen with straight line segments. These line segments are placed in the center of the specimen to clearly indicate the maximum height. After placing the cursor at the upper left hand edge of the specimen, two options are available to the analyst. Pressing either outside button on the mouse provides manual edge tracing. Pressing the center button causes the computer to go into a search mode. The six edge maps of the linear feature extraction method [Nevatia and Babu, '80] are applied to five pixels on the row immediately below the current edge. Of the five pixels, there are two pixels to the left, one below, and two to the right of the current column. Of these five pixels, the one with the largest edge strength (greatest magnitude from the six edge detectors) is identified as the new edge. This process continues while the center button on the mouse is depressed. If at any time this algorithm begins to trace a false edge, the analyst can stop by releasing the center button. An erase function is also available by depressing either outside button and moving the cursor upwards along the current edge.

This computer-assisted edge tracing method has been very successful in identifying edges of the granular material specimens. The search mode of the computer is much faster than manual tracing, but is still subject to override by the analyst. During the early stages of a triaxial test, when the edges are relatively straight, the search mode can usually identify 95-100% of an edge. In the later stages, the search mode usually identifies 80-90% of the edge. Manual tracing is used to trace the edge in regions of uncertainty where the search method identifies a false edge. This computer-assisted edge finding technique is not an elegant computer vision process, but it is quite successful in determining volume changes in the triaxial test specimens.

Magnification Correction

The presence of the water between the specimen and the confining chamber of Figure 1 creates an apparent magnification of the specimen. This magnification effect is caused by the different indices of refraction of light in the water and the plastic chamber wall. The cylindrical geometry of the test specimen and the confining chamber also requires a nonlinear mapping from the three-dimensional specimen to the two-dimensional image plane. The required mapping function is best described by an algorithm, which will be described later. The major drawback to this algorithm is that it is computationally expensive. In order to accurately map 300 rows by 200 columns in the image plane requires 60,000 passes through the algorithm, once for each pixel. Of course a smaller number of pixels could be mapped and curve fitting used, but this also requires additional computation.

Fortunately a simpler, two-dimensional model can also be developed. The physics of the test apparatus are shown in Figure 4. This model assumes that the camera can be modeled as a pinhole and there are no three-dimensional effects. Figure 4 is a true model in the plane of the pinhole camera, but is only an approximation elsewhere. Experimental results will be shown that confirm these assumptions when the distance L is "large" compared to the height of the specimen. The "image plane" is selected at the front of the confining chamber because the horizontal and vertical "inches per pixel" calibrations are easily determined at this location. The appropriate equations for the simplified model from the geometry of Figure 4 are:

$$\theta_1 = \tan^{-1}\left(\frac{X''}{L}\right) \tag{1}$$

$$\theta_a = \sin^{-1}\left(\frac{(r_3 + L)\ \sin(\theta_1)}{r_3}\right) \tag{2}$$

$$\theta_2 = \theta_a - \theta_1 \tag{3}$$

$$\theta_{1a} = \sin^{-1}\left(\frac{n_a\ \sin(\theta_a)}{n_1}\right) \tag{4}$$

$$\theta_{1w} = \sin^{-1}\left(\frac{r_3\ \sin(\theta_{1a})}{r_2}\right) \tag{5}$$

$$\theta_w = \sin^{-1}\left(\frac{n_1\ \sin(\theta_{1w})}{n_w}\right) \tag{6}$$

$$\theta_4 = \sin^{-1}\left(\frac{r_2\ \sin(\theta_w)}{r_1}\right) - \theta_w \tag{7}$$

$$\theta_3 = \theta_{1w} - \theta_{1a} \tag{8}$$

$$\theta_5 = \theta_2 + \theta_3 + \theta_4 \tag{9}$$

In these equations the indices of refraction of light in the various materials are assumed to be n_a= 1 (air), n_1=1.51 ("Lucite"), and n_w=1.33 (water). Equations 1 to 9 relate the geometrical parameters of the system to an observed horizontal position at the front of the chamber. Figure 5 shows a plot of angular position versus observed horizontal position for a value of L=24 inches. The plot shows that for small angles, i.e., near the center of the specimen, the relationship is nearly linear. Also, note that for this particular geometry it is possible to "see" an angle greater than 90 degrees. The diffraction of light in the water is responsible for this phenomenon.

In order to use Equations 1 to 9 the true specimen radius r_1 must be known. This can be determined from the observed maximum horizontal position (or edge) in Figure 4. When the angle ($\theta_4 + \theta_w$) reaches a maximum of 90 degrees, the edge appearing in the image plane (r_1") is related to the true radius r_1 by the following equations:

$$\theta_w = \sin^{-1}\left(\frac{r_1}{r_2}\right) \tag{10}$$

$$\theta_4 = 90 - \theta_w \tag{11}$$

$$\theta_{1w} = \sin^{-1}\left(\frac{n_w \sin(\theta_w)}{n_1}\right) \tag{12}$$

$$\theta_{1a} = \sin^{-1}\left(\frac{r_2 \sin(\theta_{1w})}{r_3}\right) \tag{13}$$

$$\theta_3 = \theta_{1w} - \theta_{1a} \tag{14}$$

$$\theta_a = \sin^{-1}[n_1 \sin(\theta_{1a})] \tag{15}$$

$$\theta_1 = \sin^{-1}\left(\frac{r_3 \sin(\theta_a)}{r_3+L}\right) \tag{16}$$

$$\theta_2 = \theta_a - \theta_1 \tag{17}$$

$$\theta_5 = \theta_2 + \theta_3 + \theta_4 \tag{18}$$

$$r_1'' = L \tan(\theta_1) \tag{19}$$

Figure 6 shows a plot of the calculated radius, r_1" versus the true specimen radius, r_1, along with five experimental points. The experimental values match the calculated ones

closely. Also, the relationship between true and observed radius is essentially linear in the region of specimen radii of interest (1 to 2 inches). Figure 7 shows a plot of observed radius versus true radius for several different distances L.

The two simplified models given above correct for horizontal magnification of the image. Another small correction is required for the specimen in the vertical direction. Figure 8 shows a side view of the specimen and the pinhole camera. With a large distance L the diffraction effects over the height of the specimen are small, so they are ignored in this simple model. The specimen has height h_f at the front, and height h_s along the side (where the edge is detected by the ASSIST.PAS program). By geometry the following relationship can be derived:

$$\frac{h_s}{h_f} = \frac{L + r_3 - r_1}{L + r_3} \qquad (20)$$

This correction has application in the calculation of specimen volume. Height of the specimen is best measured at the front (h_f), whereas diameter is measured along the sides. The edge tracing program identifies an edge between h_s and h_f that does not belong to the specimen (it is usually part of the platen). The pixels corresponding to this extraneous edge are discarded during the determination of specimen volume.

The development of the two-dimensional cases above will make the three-dimensional algorithm more understandable. The three-dimensional model also makes use of a pinhole camera assumption. The confining chamber is assumed to be perfectly cylindrical and oriented perpendicularly to the axis of the pinhole camera. In the algorithm given below, terms in curly braces, {X, Y, Z} are vectors in a right-handed, rectangular coordinate system. This coordinate system is rigidly attached to the confining chamber, as shown in Figure 9. According to this figure, the sequence for the algorithm is:

1) The origin of the pinhole camera is at {0, L, 0}, the image plane is at {0, r_3, 0} and is perpendicular to the Y axis.

2) Select mapping points on image plane, {X_{ip}, r_3, Z_{ip}}.

3) Extend line from origin {0, L, 0} through image plane at {X_{ip}, r_3, Z_{ip}} to outer wall using direction cosines. The equation for outer wall points is: $X_{ow}\text{^}2 + Y_{ow}\text{^}2 = r_3\text{^}2$. This forms line #1. (The points {X_{ip}, r_3, Z_{ip}} would normally be chosen at each pixel in the image).

4) The normal to the outer wall at the point of intersection is the line from the point $(0, 0, Z_{ow})$ to the point (X_{ow}, Y_{ow}, Z_{ow}). This forms line #2.

5) Lines #1 and #2 form Plane #1-2, and the angle between the lines in this plane is θ_a.

6) Angle θ_{1a} is found by the diffraction equation:
$$n_a \sin\theta_a = n_1 \sin \theta_{1a}.$$

7) Line #3 begins at (X_{ow}, Y_{ow}, Z_{ow}), lies in Plane #1-2, and is at angle θ_{1a} from Line #2 in this plane.

8) Line #3 extends to the inner wall to the point (X_{iw}, Y_{iw}, Z_{iw}). The equation for inner wall points is: $X_{iw}^2 + Y_{iw}^2 = r_2^2$.

9) The normal to the inner wall at the point of intersection is the line from the point $(0, 0, Z_{iw})$ to the point (X_{iw}, Y_{iw}, Z_{iw}). This forms line #4.

10) Lines #3 and #4 form Plane #3-4, and the angle between the lines in this plane is θ_{1w}.

11) Angle θ_w is found by diffraction equation:
$$n_w \sin\theta_w = n_1 \sin \theta_{1w}.$$

12) Line #5 begins at (X_{iw}, Y_{iw}, Z_{iw}), lies in Plane #3-4, and is at angle θ_w from Line #4 in this plane.

13) Line #5 extends to the specimen surface to the point (X_{sp}, Y_{sp}, Z_{sp}). The equation for inner wall points is: $X_{sp}^2 + Y_{sp}^2 = r_1^2$.

14) The maximum angular position observable on the specimen surface occurs when condition #13 is just barely satisfied, i.e., Line #5 is perpendicular to the specimen surface.

The point (X_{sp}, Y_{sp}, Z_{sp}) determines the true angular position of the bead located on the image plane at the point (X_{ip}, r_3, Z_{ip}).

Experimental Results

A series of three granular material triaxial tests were conducted to evaluate the computer vision measurement of volumetric strain. The results of these tests are given in Figures 10, 11, and 12. In each figure data from the conventional method for determining volumetric strain (measurement of displaced water) is plotted. Computer vision measurements were obtained from two different cameras, a front view and a side view (about 120 degrees apart). Parameters for the granular material test specimens are given in Table 1.

Table 1
Specimen Parameters

	Figure 10	Figure 11	Figure 12
Test date	6/16/87	6/18/87	6/25/87
Specimen height :	6.402"	6.612"	6.460"
Specimen diameter :	2.805"	2.805"	2.805"
Initial void ratio :	0.697"	0.637"	0.651"
Material :	3 mm glass beads		
Confining pressure :	0.2 psi		
Deformation rate :	0.021"/minute		

Figure 10 shows the worst correlation between the conventional and computer vision techniques. In the latter stages of the test the computer vision data shows a shift of approximately 1.5% volumetric strain. However, the slopes of the three sets of data do show similar trends. The digitized images of the test corresponding to Figure 10 were the lowest quality of the three experiments, possibly explaining some of the discrepancy with the conventional technique.

Figures 11 and 12 show much better agreement between the conventional and computer vision techniques. In Figure 11 the front and side view data agree within approximately 1% of volumetric strain, with the exception of one set of points at the 75 minute mark. In Figure 12 the data points before the 55 minute mark agree closely, but begin to diverge at this point. There are two possible explanations for this type of uniform divergence. First, the specimen can begin to dilate non-symmetrically, thus violating the round disk assumption of the computer vision model. Secondly, the upper platen begins to penetrate the sample at

approximately the 50 minute mark. The volume measuring algorithm assumes that the top of the specimen is stationary, so platen penetration introduces a small error in the measurement.

RGB vs. Composite Video Cameras

Two different types of color video cameras are available, RGB (red-green-blue) and composite. An RGB camera generates three RS-170 (television) signals that can be separately digitized. In a composite color camera using the NTSC standard, signals from the red, green, and blue sensors are combined to form a single RS-170 compatible output signal. The composite video signal is therefore of somewhat lower quality, since there is three times as much information available from an RGB camera. This often leads to a patterning effect when the composite video signal is displayed in "shades of gray." This patterning appears as diagonal and/or horizontal lines running across the image.

Composite video systems are also known to have some peculiarities with certain colors, notably red. Red objects appear to have a noticeable "cross-hatch" pattern associated with them. This cross-hatch pattern has been used in the bead tracing software for the identification of red tracer beads [Parker, '86]. Passing a Laplacian convolution filter over a digitized composite video image enhances the appearance of these cross-hatch patterns by converting them into vertical black and white bands. Unfortunately, the Laplacian also enhances some of the other patterns generated by the composite video signal. Careful selection of lighting and non-tracer bead color is required to successfully use this method for locating tracer beads. In particular, blue non-tracer beads give the best performance in bead tracing. However, many of the planned experiments for the granular materials project require the use of sand particles, which are an off-white color. It is difficult to "see" the red tracer beads in the white sand, even when the tracers are on the surface of the specimen.

Another problem occurs when the analyst desires to do bead tracing and volume change measurement from the same digitized image. With red tracer and blue non-tracer beads, a light background gives the best contrast for finding the specimen edges, and thusly the volume. If red tracer beads are used in white sand, then a relatively dark background would be required to give a good contrast for edge tracing. Since these experiments will (hopefully) eventually be conducted in a rarely attended, confined area of the Space Shuttle, two different backgrounds are not desirable.

The use of RGB color cameras may provide a solution to this problem. Under the right conditions, tracer beads can appear at significantly different intensities (shades of gray) in the three images from an RGB camera. Therefore lighting and background color can be optimized for specimen edge tracing and another technique used for finding the tracer beads. As an example, Figures 13 and 14 show the same region of a red and blue bead specimen. The histograms of pixel intensities in these figures have been "equalized", i.e., there are approximately the same number of pixels at each of eight gray levels. In Figure 13 most, but not all, of the light regions are red tracer beads. In Figure 14 there are significantly fewer light regions, and most of these correspond to glare from the lighting.

One way to use the two color images of the same scene is to subtract one image from the other. Figure 15 is the difference between the original images of Figures 13 and 14 (before equalizing). Note that seven tracer beads are separated and clearly identified in this figure. Another group of five touching tracer beads are also discernable. The major advantage to the subtraction method for identifying tracer beads is that it is relatively insensitive to lighting. There is a temptation to simply threshold the image of Figure 13 to find the red beads, i.e., all pixels above a certain brightness are set to white and all others to black. However, the correct threshold value would depend on carefully controlled lighting, and could vary from region to region in the image. The glare in the center of Figure 14 has been eliminated in the subtracted image of Figure 15. With simple thresholding of a single image this type of glare reduction would be difficult to accomplish.

Using RGB cameras does present a few small problems. If only two of the RGB signals are recorded (red and green for example), then twice as many video recorders or multiplexer channels will be required for the Shuttle flight hardware. Also, images to be subtracted must be from the same point in the two recordings, i.e., the must be images of the same scene. Lastly, the video systems must be well synchronized such that a point in the scene occurs at the same vertical and horizontal pixel locations in the two digitized images. Some type of registration marks could be used to correct for this type of error. Even with these additional problems, the use of RGB cameras is highly recommended.

Miscellaneous

Several miscellaneous programs have been written for use in this project. All programs using image data require the full 512x480 pixel image to be in the ImageAction non-compressed file format (*.IMG). One of the most useful is the program for printing images at eight shades of gray on the Hewlett-Packard LaserJet Plus printer (LASER_PR.PAS). This program uses the same 8x8 dot patterns defined by HP in their technical reference manual, but does not use the advanced graphics capabilities of the LaserJet (they are too slow). The program allows the user to print any selected portion of an image, up to approximately 43,000 pixels (215 columns by 200 rows). This limitation is due to the grahics limitations of the LaserJet Plus printer. Other limits are 300 columns or 360 rows due to the physical size of the paper.

Another printing program (HP_THR.PAS) prints black and white (thresholded) images in three different sizes. This program can print an entire 512x480 pixel image, provided there are not too many long vertical columns of black pixels (another limitation of the LaserJet Plus printer). One program (FULL_SIZ) can "shrink" a full 512x480 pixel image to an equivalent 213x200 pixel image and print it within the limitations of the LaserJet Plus. This program maps each 12x12 area of the original image into an equivalent 5x5 area before printing, so some details such as lines can be lost. A program for generating color pictures on the 8 pen HP 7550 plotter is also available (IMG_PLOT.PAS), but requires more than one hour of plotting time for most images.

One useful program (COLLECT.PAS) allows the user to "grab" frames at specified time intervals, either directly from the camera or from a video cassette recorder. A histogram printing program (HISTGRAM.PAS) generates a printer-plot of the pixel intensity histogram for an image. Histograms are useful for evaluating the quality of lighting used in the video system. Most computer vision algorithms perform best on an image with "good" contrast. The histogram of such an image will be spread over the entire range of pixel intensities. If the histogram is grouped near either end of the pixel intensity scale, then changes in lighting conditions are usually needed. Another program (OVERLAY.PAS) allows the user to overlay specimen edges (from a *.WID file) onto the original image. This can be useful as a subsequent check on the validity of the edge detection procedure.

Results

Most of the objectives of this project have been met. A methodology for determining volumetric changes during a granular materials triaxial test has been developed. A computer-assisted edge tracking program is used with a circular disk model to estimate the specimen volume from a digitized image. Results from this computer vision based technique show generally good correlation to conventional volumetric strain measurements.

Two models for determining the magnification effects produced by the diffraction of light in the test apparatus have been developed. The simpler of these two methods generates two linear correction factors, one each for the horizontal and vertical directions. This simplified model is adequate when the distance between the camera and the test specimen is "large" compared to the specimen height. Experimental data is provided to substantiate this claim. An algorithm is also given for generating a more accurate three-dimensional correction. The drawback to this algorithm is computational expense, but it is necessary if the camera is "close" to the test specimen.

Tracer bead tracking requires a final conversion from the two-dimensional data of the image plane to true three-dimensional position. The relationship between the observed horizontal position and the true angular position of the object depends on the local specimen diameter. Therefore, specimen diameter must be determined before this final correction can be applied (specimen diameter is estimated in the volumetric strain measurement process). Previous efforts in the tracer bead tracking effort required the use of a composite color video image of the specimen. Red tracer beads created "cross-hatch" areas that were detected by the bead locating and tracking procedures. Preliminary investigations with RGB (red-green-blue) camera signals indicate that a different method for tracer bead detection might have significant advantages. Subtracting one color image from another (green from red for example) can provide tracer bead location that is relatively insensitive to ambient lighting. Therefore lighting can be optimized for the edge tracking process.

No significant progress has been made in the evaluation of two or more "touching" beads. Initially this objective was considered a high priority. However, a different method for generating the test specimen ("raining" versus vibration) allows fairly precise placement of the tracer

beads on the surface of the specimen. Therefore few tracer beads will contact one another during the test. Work on this topic was deferred to a later date.

Recommendations

Testing of the computer vision system in a full-scale mockup of the "double locker" (17" x 20" x 20") of the Space Shuttle should be done soon. One of the critical components of any computer vision system is lighting. The current procedure to detect the edges of the specimen is especially dependent on lighting. The best system for lighting the test apparatus, the best choice of camera lenses, and the effects of background and tracer bead colors can only be determined in a full-scale system. The full three-dimensional magnification correction algorithm can also be tested in this system.

A significant difference is apparent in the quality of images digitized from a VCR (video cassette recorder) and directly from a video camera. Current VCR's have approximately half the vertical resolution of a video camera. A new generation of VCR's ("Super VHS") with approximately the same vertical resolution as a video camera is being introduced to the marketplace. If the claims are true, then this newer VCR technology should be used both in the flight mission and during ground testing.

RGB cameras offer potentially significant advantages over composite color cameras for the tracer bead tracking process. At a cost of twice as much video recording, an additional measure of independence between the requirements for "good" bead tracking and specimen edge detection can be had.

A series of tests to precisely evaluate the volumetric strain measurement procedure should be conducted. Several cylindrical specimens of well-known dimensions can be measured by the computer vision system. This would establish an absolute error baseline for this technique. There are ambiguities in the conventional measurement of volumetric strain (determination of initial specimen volume and measurement of small volumes of displaced chamber water), and this uncertainty needs to be evaluated.

Finally, a procedure for tying the two parts of the analysis (bead tracking and volumetric strain measurement) together should be developed. In particular, the specimen diameter information generated in the volumetric strain measurement analysis is needed in bead tracking for correction to true bead angular and radial position.

References

Abdou, I. E. and W. K. Pratt, "Quantitative Design and Evaluation of Enhancement/Thresholding Edge Detectors", Proceedings of the IEEE, Vol. 67, No. 5, May 1979, pp. 753-763.

Duda, R. O. and P. E. Hart, Pattern Classification and Scene Analysis, Wiley, New York, 1973.

Haralick, R. M., "Digital Step Edges from Zero Crossing of Second Directional Derivatives", IEEE Transactions on Pattern Analysis and Machine Intelligence, Vol. PAMI-6, No. 1, January, 1984, pp.58-68.

Haralick, R. M., "Edge and Region Analysis for Digital Image Data", Computer Graphics and Image Processing, Vol. 12, 1980, pp. 60-73.

Kirsch, R. "Computer Determination of the Constituent Structure of Biological Images", Computers and Biomedical Research, Vol. 4, No. 3, 1971, pp. 315-328.

Lee, J. S., R. M. Haralick, and L. G. Shapiro, "Morphologic Edge Detection", IEEE Journal of Robotics and Automation, Vol. RA-3, No. 2, April 1987, pp. 142-156.

Marr, D. and E. Hildreth, "Theory of Edge Detection", Proceedings of Royal Society of London, Vol. 207, 1980, pp. 187-217.

Nevatia, R. and K. R. Babu, "Linear Feature Extraction and Description", Computer Graphics and Image Processing, Vol. 13, 1980, pp. 257-269.

Parker, J. K. "Image Processing and Analysis for the Mechanics of Granular Materials Experiment", Proceedings of the 19th Southeastern Symposium on System Theory, IEEE Cat. #TH0180-0, March, 1987

Pratt, W. K., Digital Image Processing, Wiley, New York, 1978, pp. 478-513.

Prewitt, J. M. S., "Object Enhancement and Extraction", in Picture Processing and Psychopictorics, B. S. Lipkin and A. Rosenfeld, Eds., Academic Press, New York, 1970.

Roberts, L. G., "Machine Perception of Three-Dimensional Solids", in Optical and Electro-Optical Information Processing, J. T. Tippett et al., Eds., M.I.T. Press, Cambridge, MA, 1965, pp. 159-197.

Figure 1 - Triaxial Test Apparatus

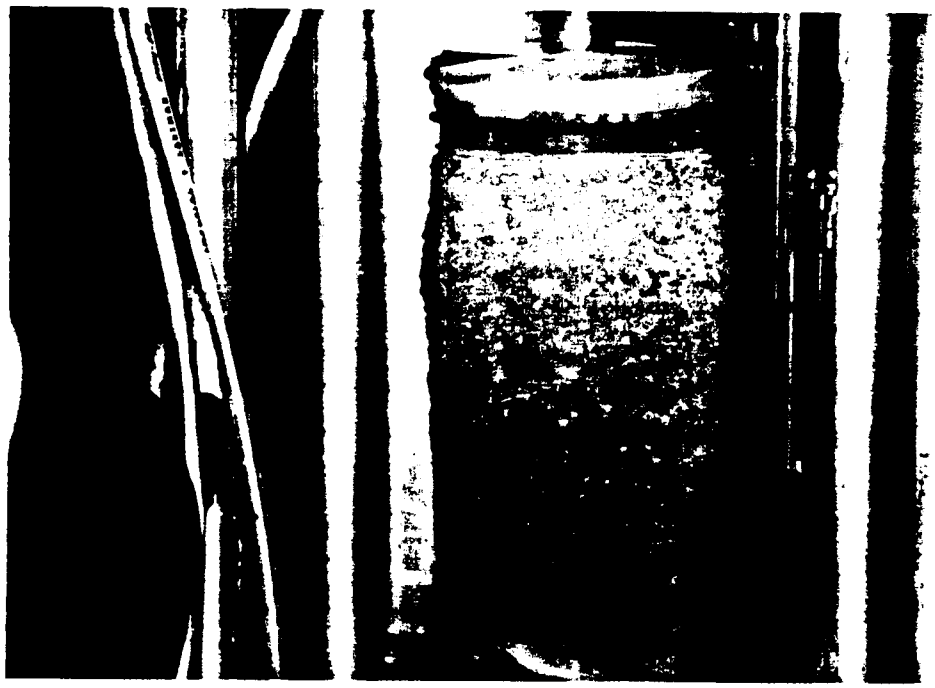

Figure 2 - Triaxial Test Specimen

Figure 3 - Computer Vision Edge Detection

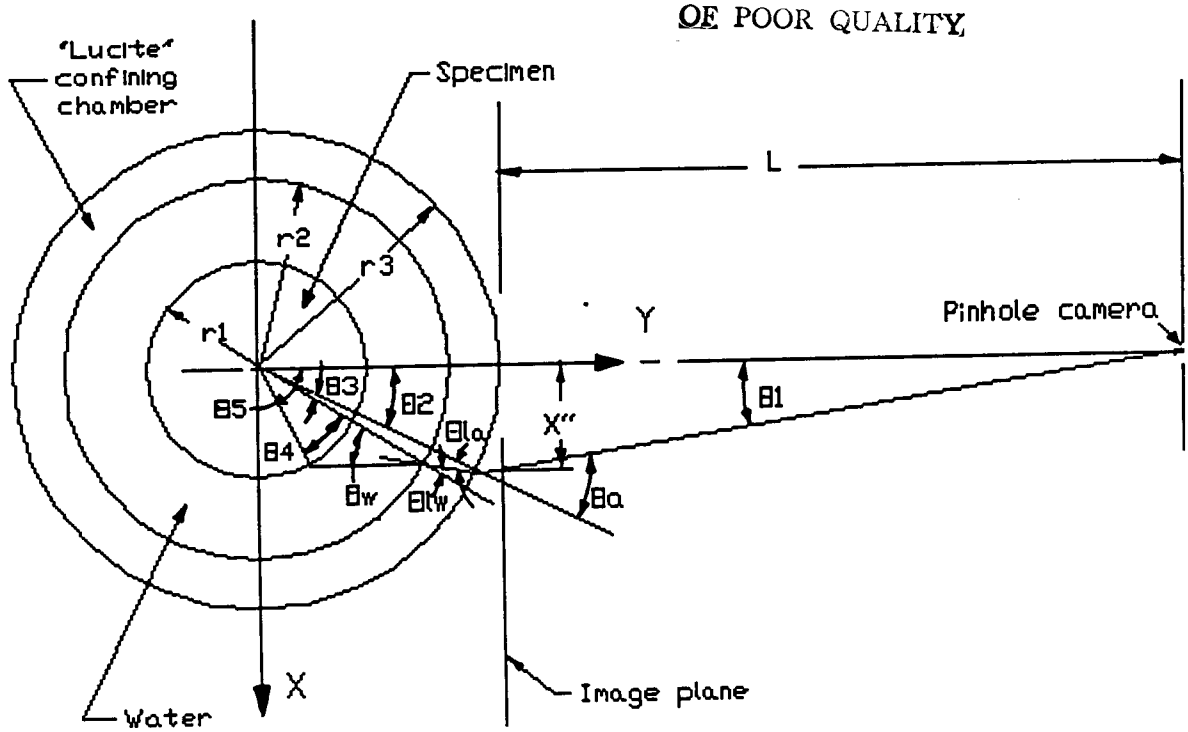

Figure 4 - Two Dimensional System Model

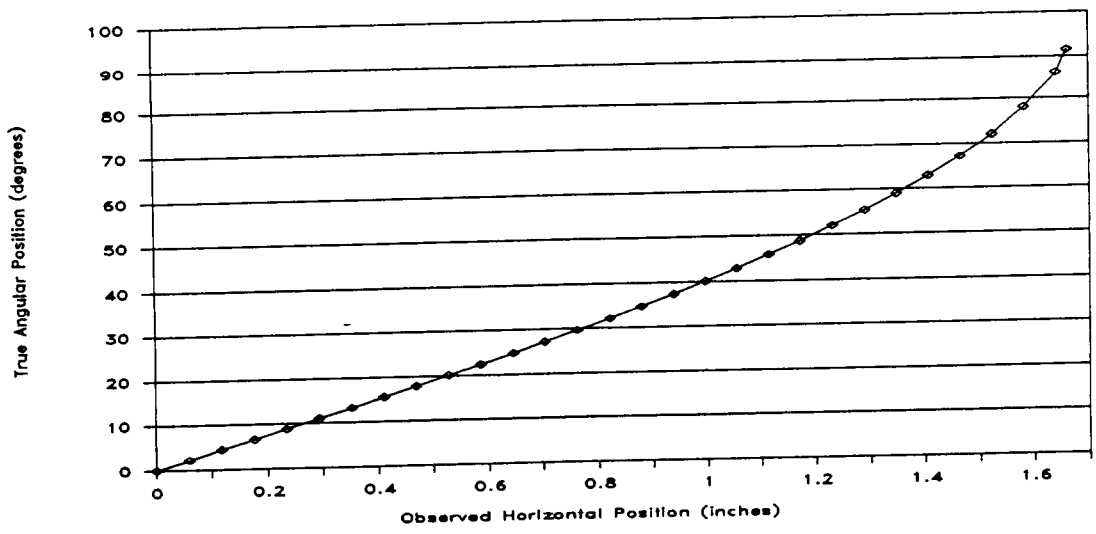

Figure 5 - True Angular Position from Observed Position

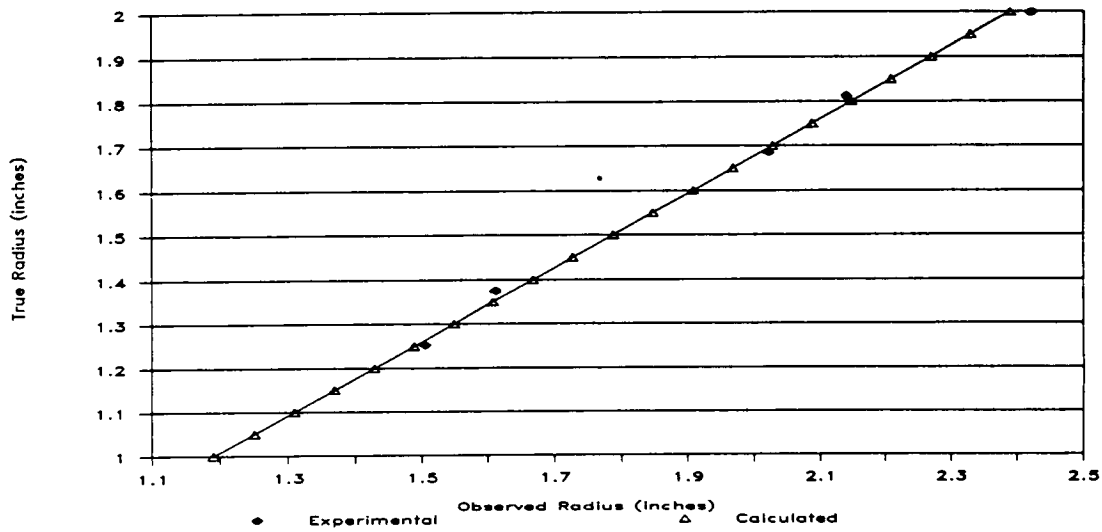

Figure 6 - Experimental and Calculated Specimen Radii

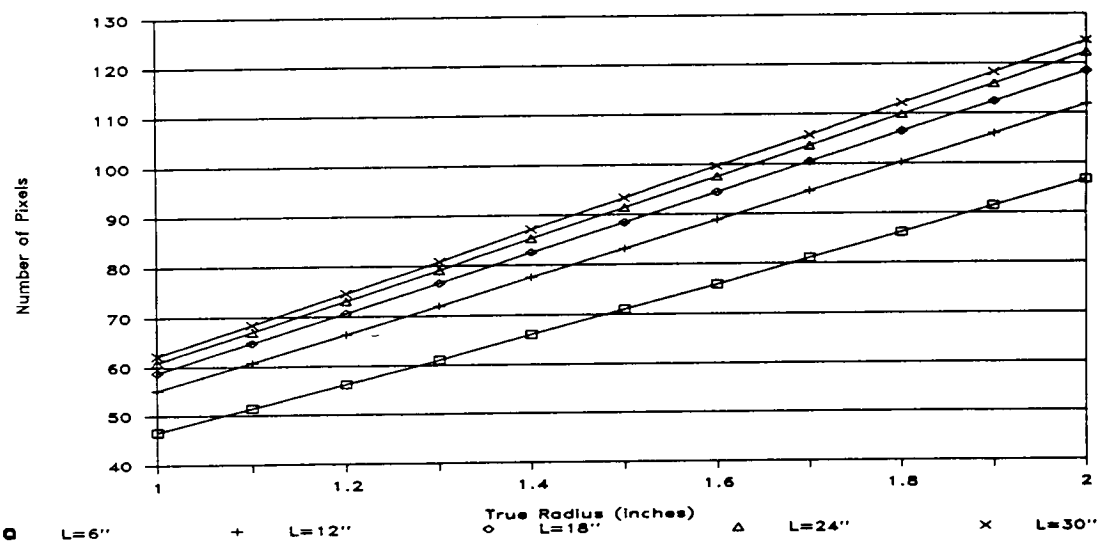

Figure 7 - True Specimen Radius from Observed Radius

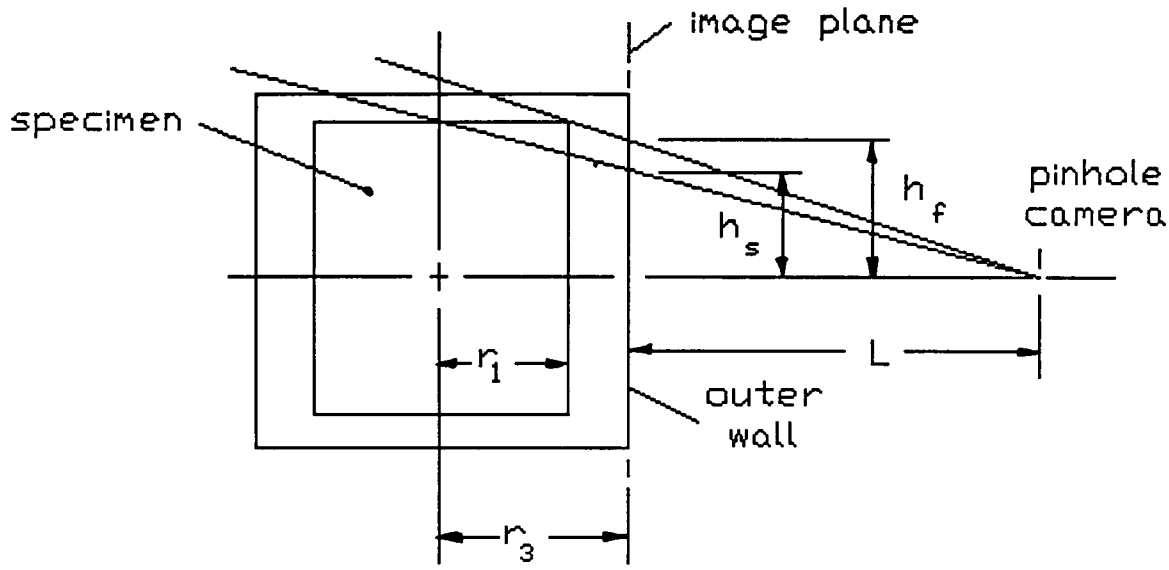

Figure 8 - Vertical Correction Model

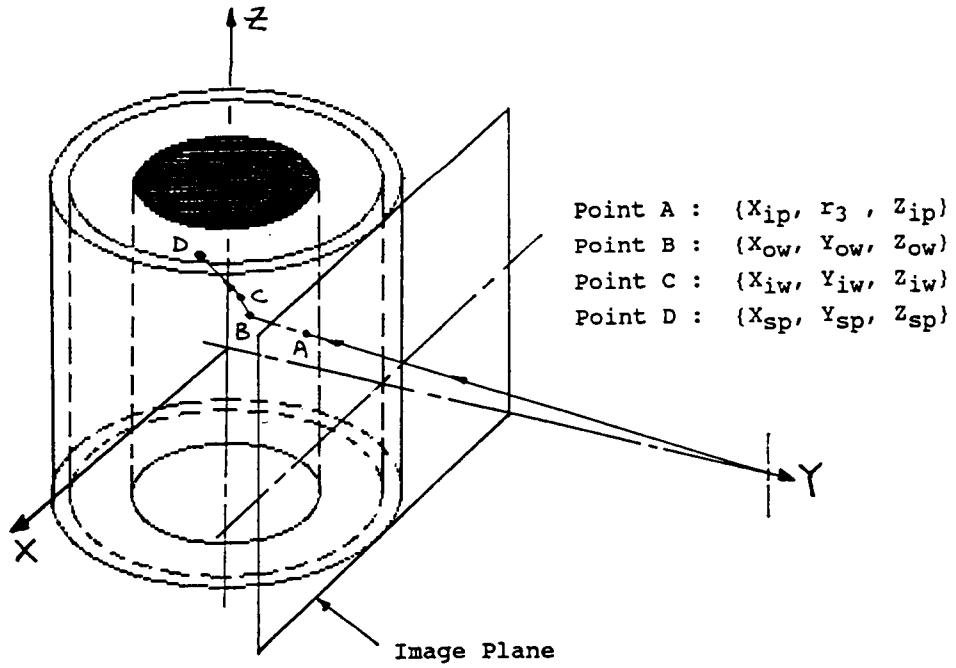

Figure 9 - Three-dimensional Magnification Correction

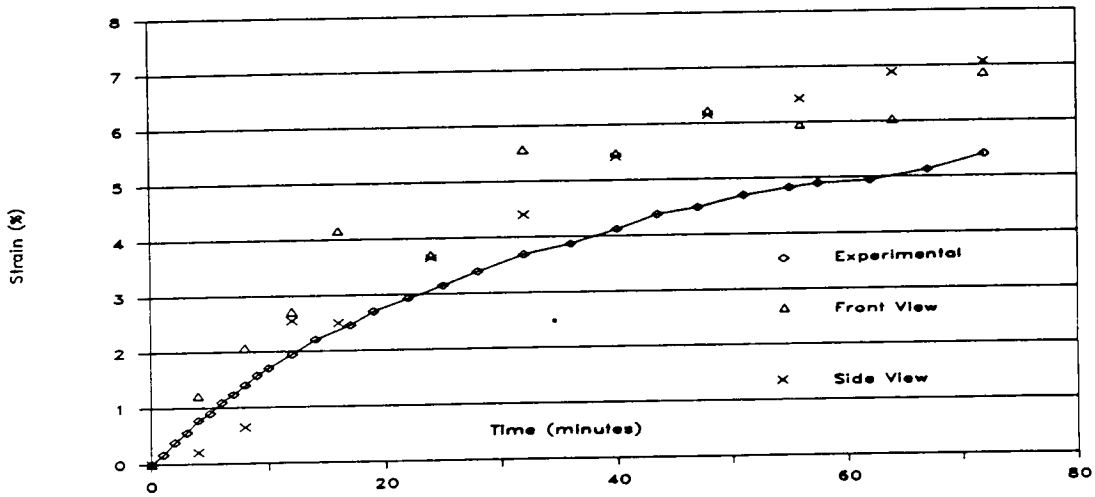

Figure 10 - Volumetric Strain Measurement (6/16/87)

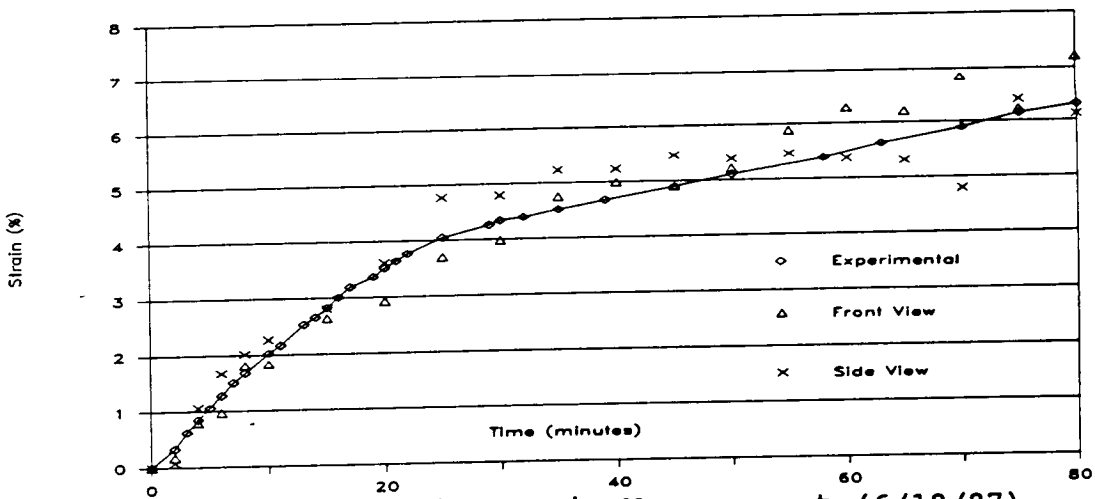

Figure 11 - Volumetric Strain Measurement (6/18/87)

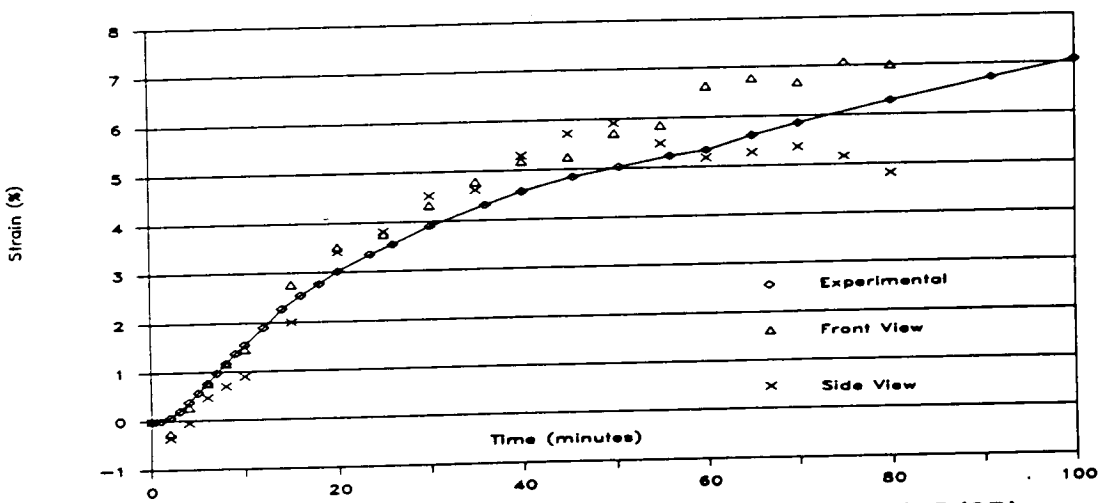

Figure 12 - Volumetric Strain Measurement (6/25/87)

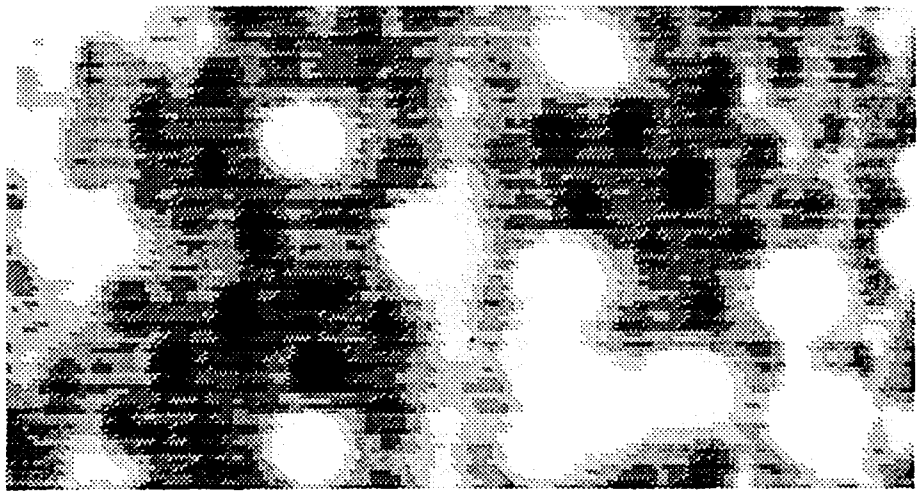

Figure 13 - Partial Image from Red Sensor

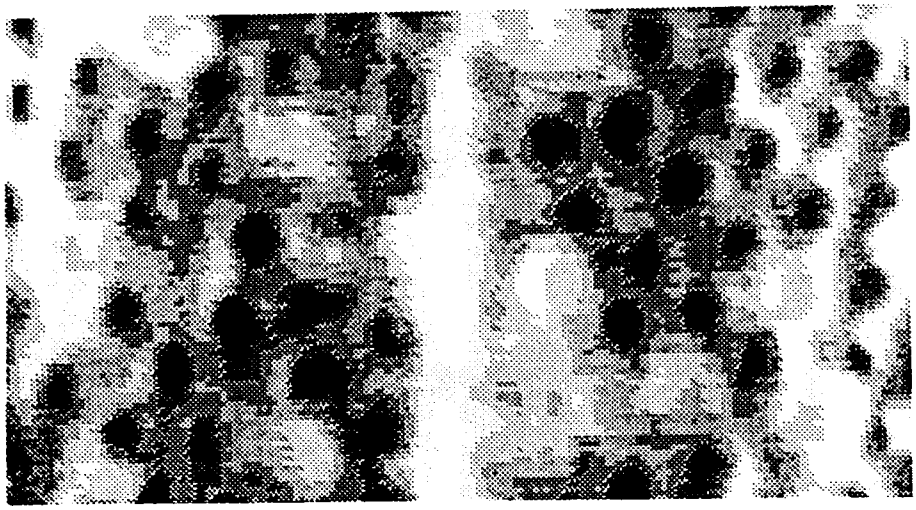

Figure 14 - Partial Image from Green Sensor

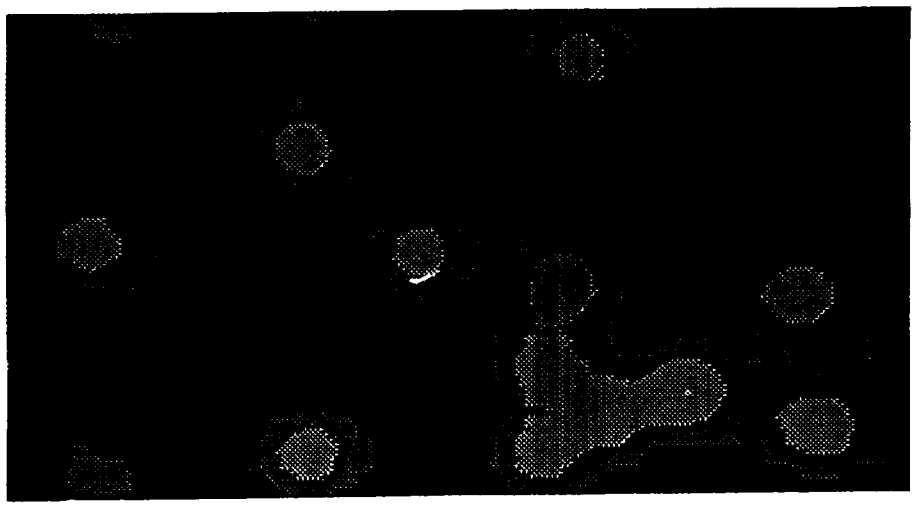

Figure 15 - Subtracted Partial Images